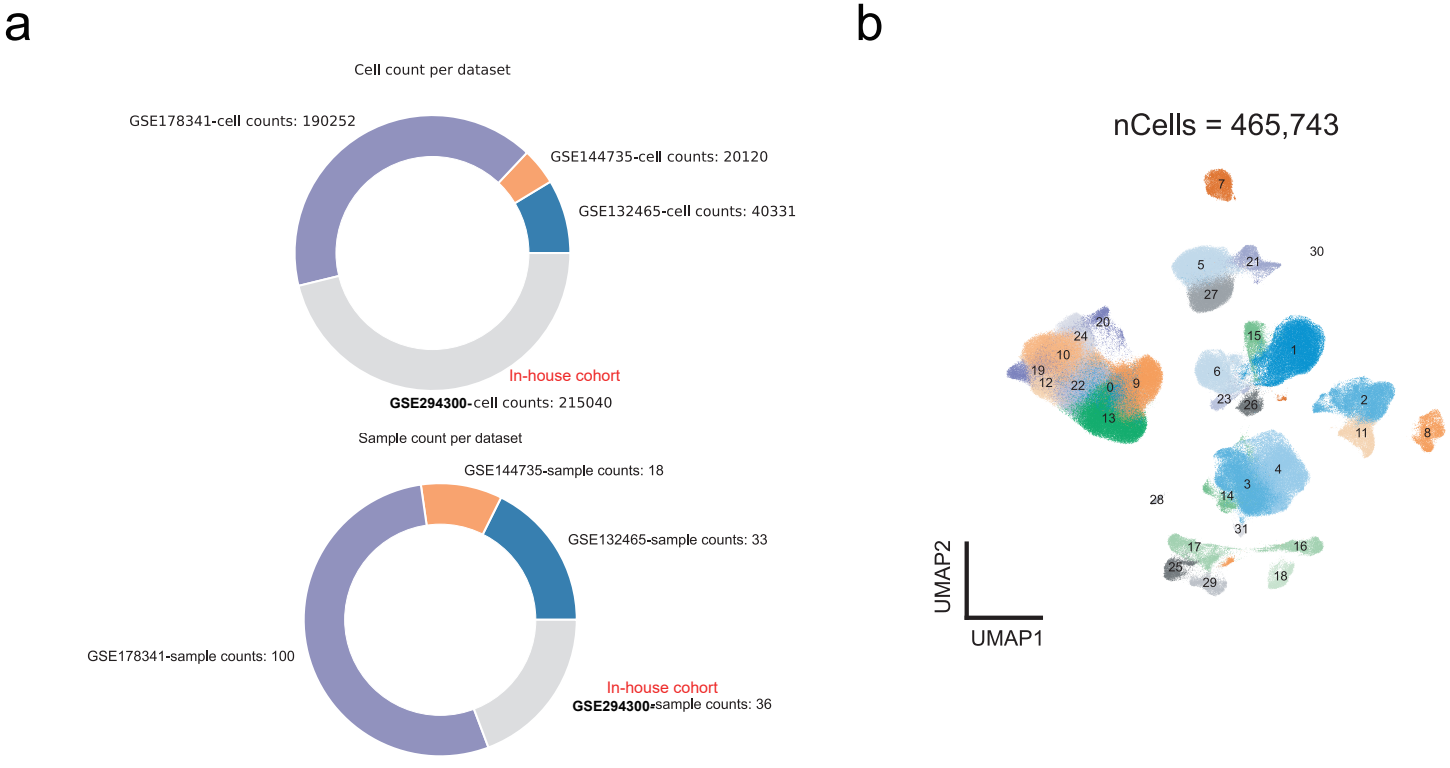

Supplementary Figure 1. Generation and annotation of the integrated single-cell atlas.
a. Pie chart depicting the composition of the single-cell dataset. The chart illustrates the total number of cells analyzed and patients enrolled in this study.
b. UMAP visualization of cellular heterogeneity. Cells are colored according to their cluster assignment, revealing distinct cell populations identified through unsupervised clustering.

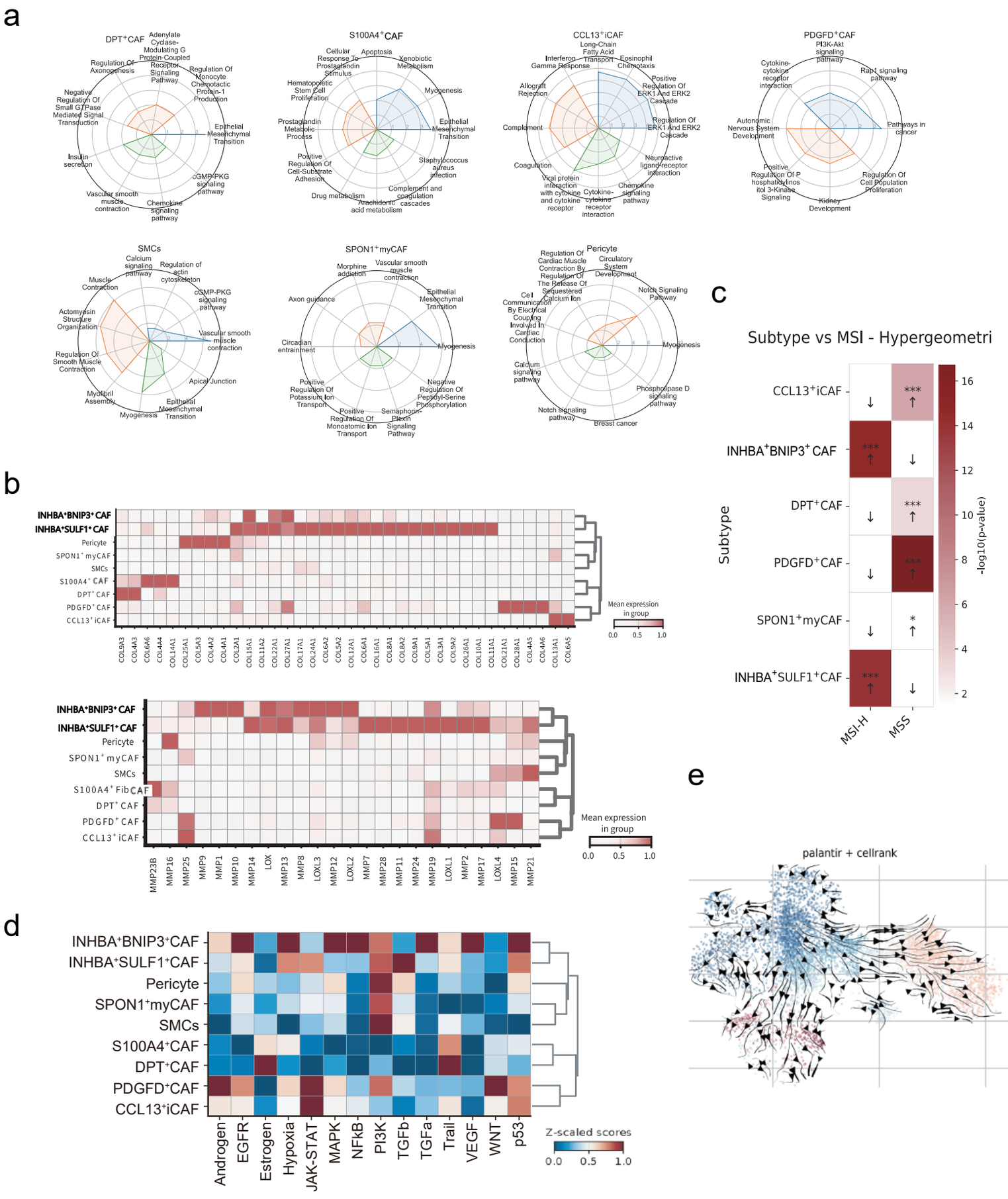

Supplementary Figure 2. Functional heterogeneity and lineage dynamics of CAF subtypes.
a. Radar plots illustrating distinct KEGG pathway enrichment patterns derived from subtype-specific differential gene expression.
b. Heatmap showing the mean expression of lipoxygenase (LOX)- and matrix metalloproteinase (MMP) associated genes and collagen (COL)-associated genes
c. Proportion of CAF subtypes in tumors stratified by microsatellite instability (MSI) status (MSI-H, microsatellite instability-high; MSS, microsatellite stable).
d. PROGENy pathway activity scores across CAF subtypes
e. Developmental trajectories of fibroblast subsets inferred by Cell2fate, visualized on UMAP.

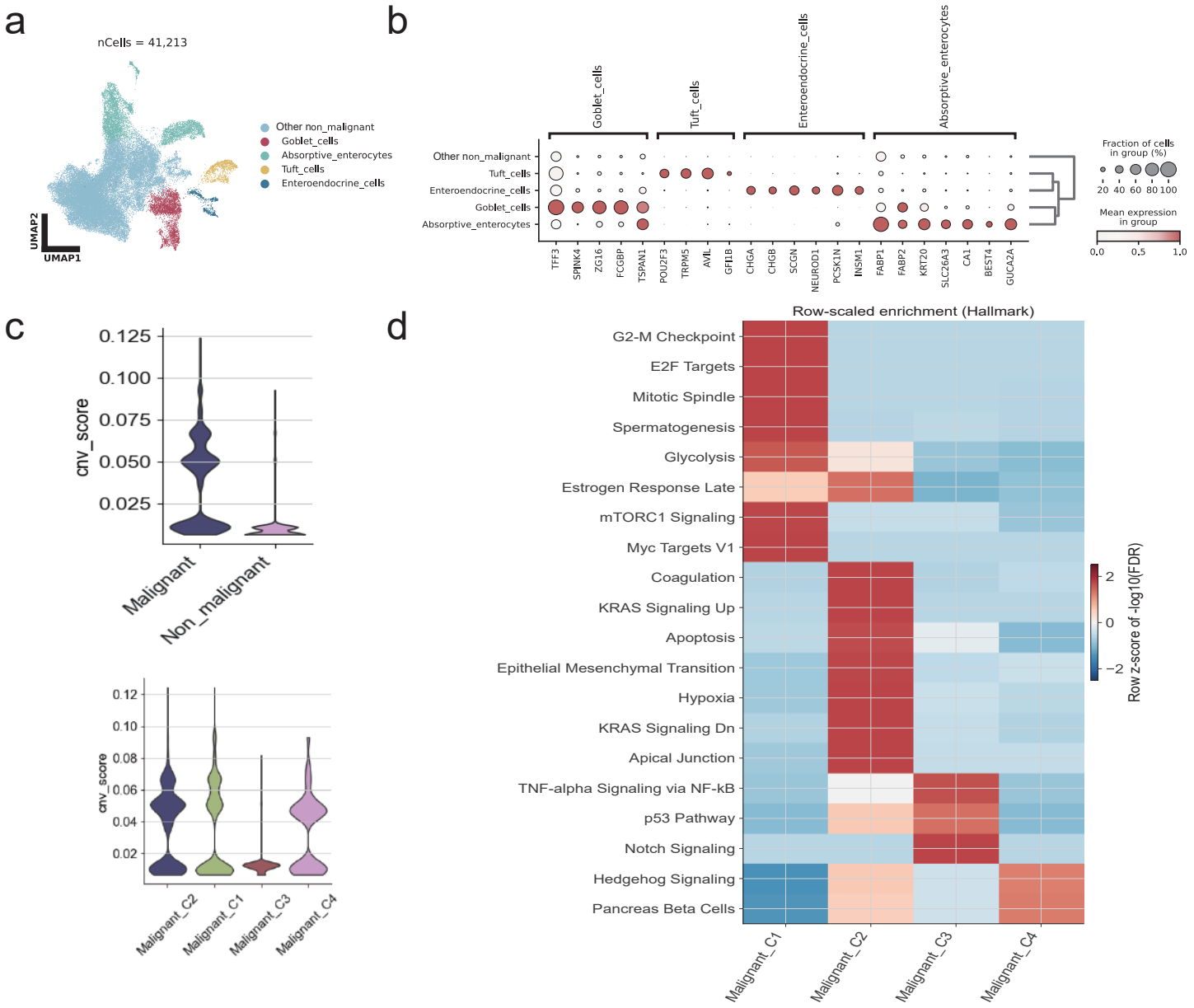

Supplementary Figure 3. Single-Cell Transcriptomic Atlas of Non-Malignant and Malignant Epithelial Cells in CRC.
a. UMAP visualization of five non-malignant epithelial cell subtypes, with different colors representing different subtypes.
b. Dot plot of highly variable genes across non-malignant epithelial subtypes.
c. CNV scores in epithelial cells, comparing malignant versus non-malignant populations (left) and distribution across malignant subtypes (right).
d. Heatmap of Hallmark pathway enrichment scores in malignant epithelial cells.

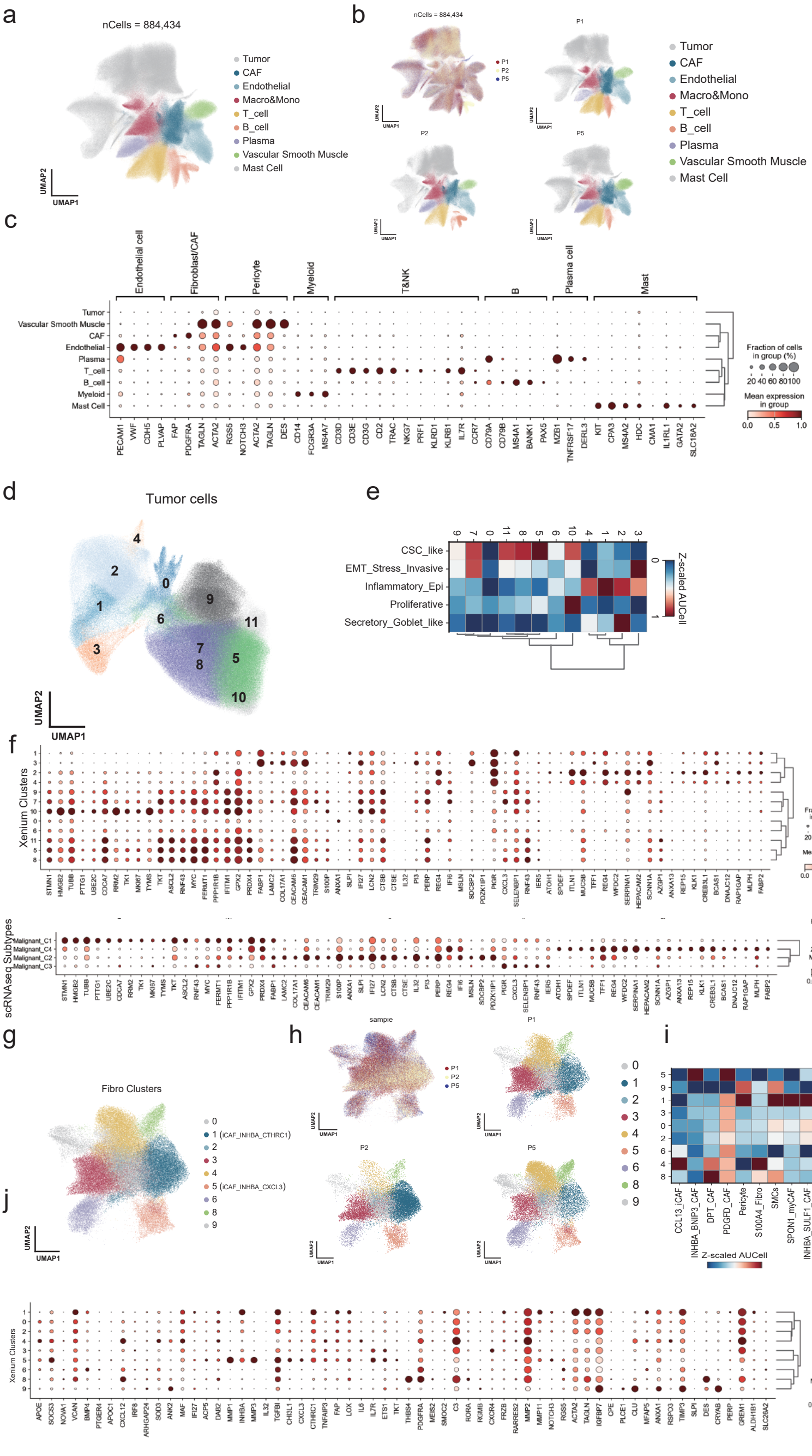

Supplementary Figure 4. Dissecting the TME with Xenium: cellular heterogeneity and subcluster-specific programs

a. UMAP projection illustrating the distribution of all cellular subtypes within the Xenium cohort.

b. UMAP visualization of total cells from three patients, colored by patient origin and major cell types.

c. Dot plot showing the expression of marker isoforms across all identified cell types, based on Xenium data.

d. UMAP visualization of malignant cell subclusters from the Xenium cohort. Cells are colored by their cluster assignment, revealing distinct populations defined through unsupervised clustering.

e. Z-scored AUCell values were calculated across malignant cell subclusters within the Xenium cohort.

f. Comparison of key epithelial marker expression between single-cell and Xenium spatial data across subclusters.

Supplementary Figure 5. Spatial niche composition in CRC samples
a. Cellular neighborhood mapping within the CRC TME.
b. Median cell-type composition across spatial niches in CRC.
c. Spatial co-localization of Malignant C2 cells and INHBA$^+$SULF1$^+$ CAFs in CRC.
d. Spatial co-localization of CD4$^+$ Treg cells and INHBA$^+$BNIP3$^+$CAFs in CRC.
e. Spatial co-localization of Malignant C2 cells and INHBA$^+$BNIP3$^+$CAFs in CRC.
f. Venn diagram showing overlap of top five CAF and malignant cell subtypes in niche 4.
g. Circos plot summarizing the number and strength of interactions across all cell types.
h. Bubble chart displaying specific receptor-ligand interactions between CAF subtypes and malignant epithelial subtypes.

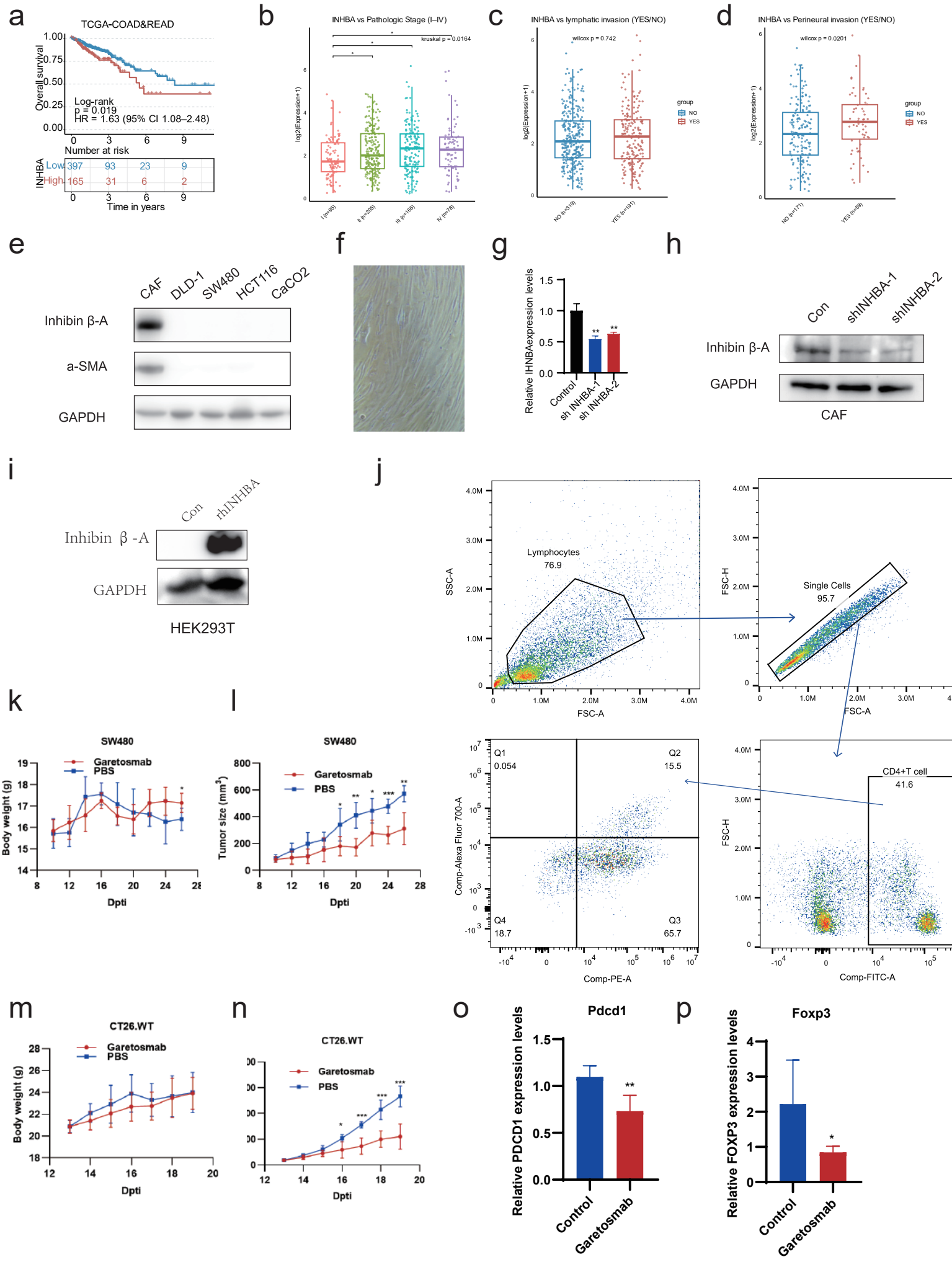

Supplementary Figure 6. INHBA contributes to the progression of CRC.

a. Kaplan – Meier analysis of overall survival (OS) stratified by INHBA expression in TCGA-COAD&READ (Log-rank test).

b. Correlation of INHBA expression with tumor stage in TCGA-COAD&READ (Mann-Whitney U test, *p < 0.05, **p < 0.01).

c-d. Association between INHBA expression and c, perineural invasion; d, lymphatic invasion in TCGA-COAD&READ (Mann-Whitney U test).

e. Protein levels of α-SMA and inhibin β A (INHBA) in CAFs and CRC cells, assessed by Western blot.

f. Representative images of CAF after initiation of culture.

g-h. Validation of INHBA knockdown efficiency by shRNA in primary CAFs, as assessed by qRT-PCR (g) and Western blot analysis (h).

i. Efficiency of INHBA overexpression in HEK293T cells, assessed by Western blot analysis.

j. Representative flow cytometry plots showing the gating strategy for CAF and PBMC co-culture. One representative sample is shown.

k-l. Mice co-implanted with CAFs and tumor cells were monitored for tumor volume (k) and body weight (l) over time. Data are mean ± SD (n=5). *p < 0.05, **p < 0.01, ***p < 0.001 vs. control.

l-m. Mice implanted with CT26.WT tumor cells were monitored for tumor volume (l) and body weight (m) over time. Data are mean ± SD (n=5). *p < 0.05, **p < 0.01, ***p < 0.001 vs. control.

n-o. Tumor tissues from the CT26.WT model mice were collected at the endpoint, and expression levels of Foxp (n) and Pdcd1(o) were analyzed by qPCR. Data are mean ± SD (n=5). *p < 0.05, **p < 0.01 vs. control.